MODELAIR – DELIVERABLE

D3.2 – NUMERICAL DATABASES (VELOCITY FIELDS)

This report is part of a project that has received funding from the European Union's Horizon Europe MSCA Doctoral Networks 2021 programme under **Grant Agreement No. 101072559**

Deliverable number: D3.2

Due date: 15 December 2024

Type[1]: O

Dissemination Level[1]: PU

Work Package: WP3

Lead Beneficiary: KTH Royal Institute of Technology

Contributing Beneficiaries: Barcelona Supercomputing Center

1

Type	R = Report	ADM = Administrative	PDE = diss./ex.	O = Other
	DEC = Websites, patents filing, press & media actions, videos, etc.			
Dissemination Level	PU = Public			
	CO = Confidential, only for members of the consortium (including the Commission Services)			
	CI = Classified			
	SEN = Sensitive, limited under the conditions of the Grant Agreement			

DOCUMENT HISTORY

Deliverable leader: Ricardo Vinuesa

E-mail of lead author: rvinuesa@mech.kth.se

Reviewer(s): Oriol Lehmkuhl

Version	Date	Description
0.1	15/11/2024	Draft
0.2	20/11/2024	Review
1.0	25/11/2024	**Final version**

Abstract:

In this deliverable we discuss the numerical simulations of simplified urban environments produced for the rest of the MODELAIR project. In particular, we discuss simulations of one obstacle and multiple obstacles with different heights with the CPU-based code Nek5000, and all the development work required to conduct simulations with the GPU-based code SOD2D.

Keywords: Numerical simulation, Turbulence, Urban flow, CPU, GPU

Acronyms

AP: Associated Partner

BEN: Beneficiary

CFD: Computational fluid dynamics

COO: Coordinator

CPU: Central processing unit

DNS: Direct numerical simulation

GLL: Gauss–Lobatto–Legendre

GPU: Graphics processing unit

LES: Large-eddy simulation

PDE: Partial differential equation

RANS: Reynolds-averaged Navier-Stokes

SEM: Spectral-element method

TBL: Turbulent boundary layer

TKE: Turbulent-kinetic-energy

ZPG: Zero-pressure-gradient

List of Participants

1	COO	Universidad Politécnica de Madrid	UPM	ES
2	BEN	BARCELONA SUPERCOMPUTING CENTER-CENTRO NACIONAL DE SUPERCOMPUTACION	BSC	ES
3	BEN	UNIVERSITE LIBRE DE BRUXELLES	ULB	BE
4	BEN	KUNGLIGA TEKNISKA HOEGSKOLAN	KTH	SE
5	BEN	OVE ARUP & PARTNERS SA	ARUP	ES
6	BEN	MICROFLOWN TECHNOLOGIES BV	MT	NL
7	AP	BuildWind SPRL	BW	BE
8	AP	BRISTOL CITY COUNCIL	BRIS CC	UK
9	AP	AYUNTAMIENTO DE MADRID	AY MAD	ES
10	AP	UNIVERSITY OF BRISTOL	UoB	UK
11	AP	AIR QUALITY CONSULTANTS LTD	AQC	UK

Table of Contents

NUMERICAL DATABASES (VELOCITY FIELDS)

1. Introduction

Rapid urbanization has introduced numerous challenges in developing urban infrastructure, necessitating innovative approaches to manage and mitigate the impacts on urban environments. Among these challenges, understanding wind patterns and coherent structures within the urban canopy has become crucial, given their profound implications for urban dynamics.

Wind patterns within cities play a significant role in pollution dispersion, directly impacting urban air quality (Torres et al., 2021). Moreover, they influence the efficiency of emerging technologies such as drone transportation services, affect the distribution and intensity of heat waves, and impact urban ventilation systems and the overall urban microclimate. With the World Health Organization projecting that air pollution in cities contributes to 7 million premature deaths annually (and 800,000 in Europe only) (Lelieveld et al., 2019), gaining insights into these wind behaviors is essential not just academically but as a practical necessity. Enhanced understanding of these patterns is essential for optimizing urban planning, improving public health, and ensuring the success of technological innovations in urban spaces. Traditionally, insights into these complex wind fields have been obtained by deploying sensors within the urban canopy. This approach, while providing valuable empirical data for modelling and predicting wind behavior, is often economically expensive. Such data has been instrumental in helping urban planners and engineers make informed decisions.

Fluid flows, including urban wind fields, are governed by the Navier–Stokes equations, a set of nonlinear Partial Differential Equations (PDEs). Numerical approaches, such as Reynolds-averaged Navier–Stokes (RANS), large-eddy simulation (LES) and direct numerical simulation (DNS) can be used to analyze these vortical structures by solving the PDEs within a defined domain. RANS, often used to study general flow phenomena, provides a spatially averaged flow field, which limits the detail available about turbulent dynamics. In contrast, LES and DNS offer high-fidelity spatiotemporal simulation data that capture the chaotic turbulent dynamics across extensive scales. High-resolution LES is particularly advantageous, as it solves the equations with almost no approximations, providing a detailed understanding of complex flow structures within urban environments. High-resolution large-eddy simulation (LES) is an approach that enables resolving the details of the turbulent flow in such environments with very high level of detail, at an affordable computational cost. In particular, our turbulence statistics are in excellent agreement with fully resolved direct numerical simulations (DNSs), and the computational cost is reduced by a factor of 10.

In this document we describe 3 types of simulations conducted to produce a complete database of urban-flow data, to be used by the rest of the consortium in a wide range of analyses:

- DNS of the turbulent flow around one obstacle, using the CPU-based spectral-element code Nek5000.

- High-resolution LES of the turbulent flow around two obstacles in tandem, where the obstacles have different heights. These are also conducted using Nek5000.
- Development of the analysis techniques to compute turbulence statistics and initial simulations of pressure-gradient turbulent boundary layers using the GPU-based spectral-element code SOD2D.

The various simulations will be discussed next.

2. One-obstacle simulations

Despite the advantages of DNS in generating high-fidelity turbulent flow datasets, it requires an exorbitant amount of computational resources to achieve the necessary resolution for solving these PDEs. Hence, to reduce flow-field variations due to geometrical intricacies, we have performed the DNS simulation of a wall-mounted square obstacle, which serves as a simplified representation of an urban environment, specifically simulating flow around a building. The spectral-element-method (SEM)-based open-source code Nek5000 developed by Fischer et al. (2008) is used to solve the incompressible Navier-Stokes equations:

$$\nabla \cdot \boldsymbol{u} = 0,$$

$$\frac{\partial \boldsymbol{u}}{\partial t} + \boldsymbol{u} \cdot \nabla \boldsymbol{u} = -\nabla p + \nu \nabla^2 \boldsymbol{u},$$

Here, u represents the three-component velocity field in the streamwise (x), wall-normal (y), and spanwise (z) directions, while ν and p denote viscosity and pressure, respectively. Detailed information regarding the data generation process is available in Martínez-Sánchez et al. (2023).

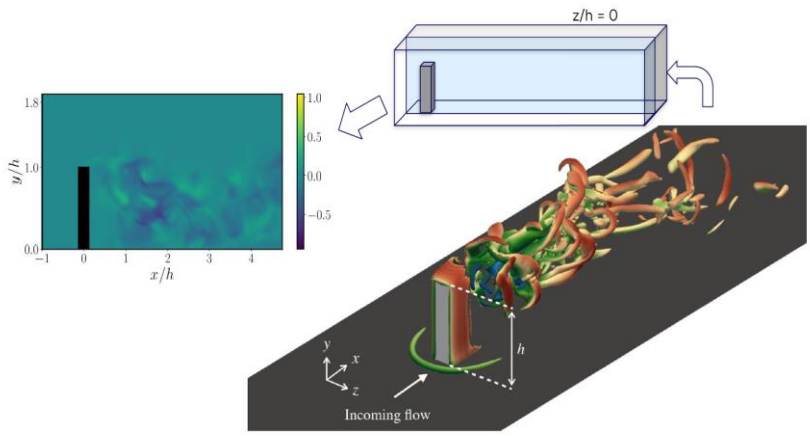

Figure 1: Instantaneous visualization of the flow around a wall-mounted square obstacle (Martinez-Sanchez et. al., 2023) and extraction of velocity fluctuations at a 2D plane from the 3D domain at z/h =0

In the spectral-element method (SEM) (Patera, 1984), the computational domain is divided into discrete elements, with the solution represented using Lagrange interpolants of order N within each element. The nodes within these elements are arranged according to the Gauss–Lobatto–Legendre (GLL) distribution. An isoparametric mapping is used to define the shape of each element, with no restrictions on their positioning within the domain. This flexibility allows SEM to handle complex geometries effectively while maintaining the advantages of a high-order spectral method. In this study, the velocity field is represented using Lagrange interpolants of order N=5, while the pressure field is approximated with order N-2 = 3. Nonlinear terms are treated explicitly through third-order extrapolation (EXT3), and viscous terms are handled implicitly using a third-order backward differentiation scheme (BDF3). A no-slip boundary condition is applied along the cylinder walls and ground, with periodic boundary conditions set in the spanwise direction. At the top boundary, we impose a constant streamwise velocity, zero spanwise velocity, and zero shear stress in the wall-normal direction. The inflow is a laminar boundary layer, while the outflow uses the stabilized boundary condition proposed by Dong et al. (2014).

The square obstacle in the simulation has a width-to-height ratio (b/h) of 0.25, with all geometric dimensions normalized by the obstacle height, h. The simulation is conducted at a Reynolds number of 2000, based on the obstacle height, under a laminar inflow boundary layer. A spectral element mesh with 21.8 million grid points is used to capture the flow dynamics accurately. A computational domain near the obstacle is extracted from this mesh with bounds of $-1 \le x/h \le 5$, $0 \le y/h \le 20$ and $-1.5 \le z/h \le 1.5$. The data is then interpolated onto a uniform mesh with a resolution of (Nx, Ny, Nz)=(300, 100, 150). Temporal parameters are expressed in convective time units, defined by the ratio of free-stream velocity U_∞ to the obstacle height. A constant time step $\Delta ts=0.005$ is used between snapshots, providing sufficient temporal resolution to capture both low- and high-frequency flow phenomena, as identified by Martinez-Sanchez et al. (2023).

Only statistically stationary fields are stored, with transient time steps removed from the data. A total of 50,000 snapshots are obtained, corresponding to 250 convective time units. Additionally, a two-dimensional dataset of velocity fluctuations is extracted from the three-dimensional fields at the midplane, as shown in Figure 1. This two-dimensional dataset offers researchers an efficient way to develop new data-driven methods, which can then be extended to the full three-dimensional dataset.

3. Two-obstacle simulations

Here we summarize the high-resolution LESs conducted to investigate the interaction between two square, wall-mounted cylinders immersed in a zero-pressure-gradient (ZPG) turbulent boundary layer (TBL) and the analysis of the turbulence structures. The study focuses on two obstacles arranged in a tandem configuration, with the heights of the cylinders denoted as h_1 and h_2, respectively, as depicted in Figure 2.

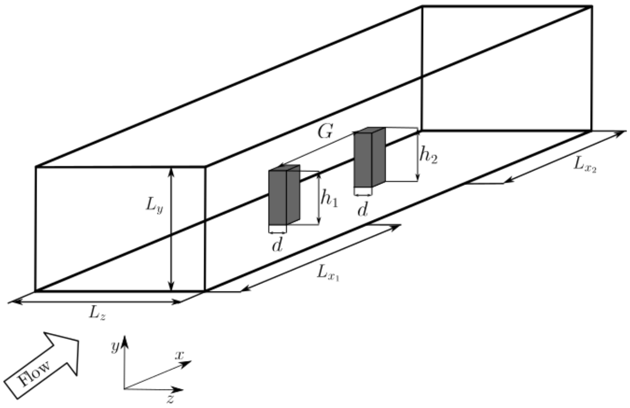

Figure 2: Sketch of the computational domain, which has dimensions $L_{x_1} = 10h_1$, $L_{x_2} = 6h_1$, $L_y = 3h_1$, and $L_z = 4h_1$.

The spacing between the two obstacles is denoted as G. All quantities are normalized by the upstream building height h_1 and the free-stream velocity u_∞, while the time is normalized by h_1/u_∞. The values of G/h_1 are set to 1.25, 2.25, and 4.25, corresponding to the configurations "SF," "WI," and "IR" from Atzori (2023), referred to as "Skimming Flow," "Wake Interference," and "Isolated Roughness," respectively.

The aspect ratio (AR) is defined as the ratio between each building's height and width. The upstream building has AR=2, while the downstream building has AR=1. This implies that $h_2/h_1 = 0.5$. Both buildings are immersed in an incompressible turbulent boundary layer, where the friction Reynolds number upfront the leading cylinder is $Re_\tau = u_\tau \delta/\nu = 180$, where ν is the kinematic viscosity, where the friction velocity is $u_\tau = \sqrt{\tau_w/\rho}$. For all configurations, the oncoming flow is the same. This approach allows us to focus on the geometrical effect, disregarding the influence of turbulence intensity on the time-averaged turbulent wake structures. This work aims to highlight differences and similarities across a series of different configurations involving an isolated wall-mounted cylinder (case AR2), two identical cylinders in tandem (cases SF, WI and IR from Atzori, 2023) and the current cases with $h_1 = 2h_2$, denoted with the label "21". All the cases are summarized in Table 1.

Case name	h_1	h_2	G	Sketch
AR2	1	-	-	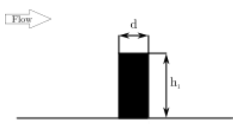

SF	1	1	1.5	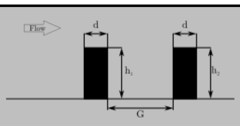
WI	1	1	2.5	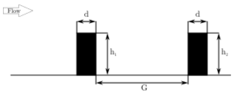
IR	1	1	4.5	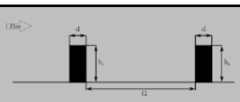
SF21	1	0.5	1.5	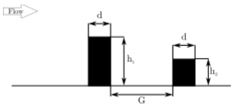
WI21	1	0.5	2.5	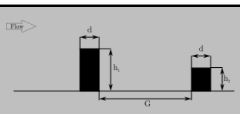
IR21	1	0.5	4.5	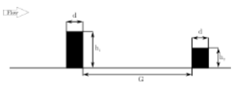

Table 1: Summary table of all the configurations studied.

The changes in distance G and obstacle height h_2 concern several points:

1. **Wake turbulent structures**: When the downstream cylinder is shorter and for the narrow regime (case SF21) the wake extends above the rear cylinder. Only the lower part of the wake is affected, while the outer region exhibits a recirculation bubble similar to that of the case AR2. However, the screening effect, initially observed for the case SF, diminishes. As the gap widens (WI21 and IR21), flow interactions between the cylinders weaken, while the upper wake freely develops. In addition, the distribution of Ω_x downstream the leading cylinder for the WI21 case shows stronger vortices that can be comparable to base vortices, not displayed for WI. This effect emphasizes the influence of the rear obstacle on the lower portion of the leading-cylinder wake. Our findings suggest that the conventional classification of skimming flow, wake interference, and isolated roughness does not fully apply when the two obstacles differ in height.

2. **TKE distribution:** TKE peaks within the wake of the leading cylinder. However, its peak size reduces due to the rear cylinder's blockage effect, especially in SF and SF21 configurations. The shorter h_2 causes the TKE peak to further extend above the rear obstacle, affecting the turbulence production and transport downstream the rear cylinder. Increasing the gap enhances TKE between the cylinders and allows a higher-energy flow from the outer boundary layer to penetrate within the gap, (see WI21 and IR2).

3. **Integral of the TKE budget:** In order to quantify the overall influence of the rear obstacle, we introduced the integral quantities such as the volumetric integral of K and P^k. The quantity selected highlights that the SF and SF21 cases produce lower turbulence levels, while the WI case remains closest to the reference AR2. The reduction in turbulence in the wake for smaller gaps (SF) and the increased turbulence production with increasing gap size (WI21, IR21) align with the findings from the integral analysis.

The present analysis investigates how the variation in obstacle height and separation alter velocity and turbulence patterns, and thus affect the classification of the flow regimes for wall-mounted cylinders in tandem. We observed that SF regime definition becomes problematic; flow no longer "skims" but detaches at the roof trailing edge, resembling WI characteristics. The SF21 case, with a smaller h2h_2h2, resembles WI rather than SF, suggesting it could fit within the WI regime. In SF and SF21 cases, turbulence production PkP_kPk peaks at the rear obstacle's leeward side, suggesting an intensified turbulence impact. Reduced h_2 in WI cases strengthens vortices from the leading cylinder, forming the strongest structures around $x = 2$. The classification becomes impractical for cases with varying obstacle heights, suggesting further study with intermediate heights and Reynolds numbers.

Note that the mean streamlines from the three cases with different obstacle height are shown in Figure 3. This figure illustrates the main changes in flow behavior in the three cases with different obstacle heights.

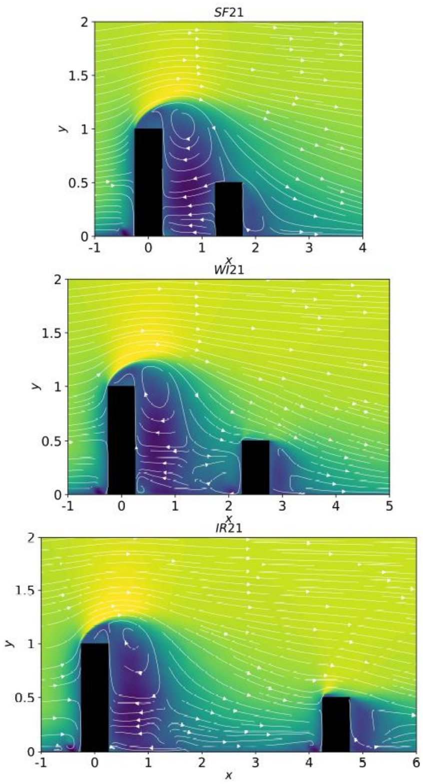

Figure 3: Mean streamwise velocity at z/h=0 and mean streamlines in white for the three cases with different obstacle heights.

4. Developments with SOD2D

Part of the work developed in this project involved implementing a toolbox to calculate all the turbulence statistics in SOD 2D on the fly. This means that the terms required to compute all the turbulent-kinetic-energy (TKE) budgets are collected as the simulation is running, and all the necessary averaging processes are carried out in a post processing step. This enabled setting up some initial boundary-layer simulations involving streamwise pressure gradients, which can be very important in case that additional urban-flow cases are required when developing machine-learning models in the rest of the project. In this case, the present SOD2D setup is ready to conduct such simulations.

Turbulence statistics in SOD2D. From the point of view of gaining physical understanding of turbulent flows, it is convenient to describe the flow in terms of its statistical properties, as it is seldom necessary to know all the intricate details of the flow field. We developed a post-processing framework in SOD2D code where all the quantities required to compute the Reynolds stresses budgets as well as 1st to 4th order one-point statistics can be calculated during the runtime, thus obviating the need to post-process the instantaneous snapshots saved individually. The post-processing toolkit can compute the statistical quantities for 3D inhomogeneous flows and for flows having 1 or more homogeneous directions. In Figure 4 we present the mean flow statistics of channel flow at $\boldsymbol{Re_\tau = 180}$ obtained using our post-processing toolkit.

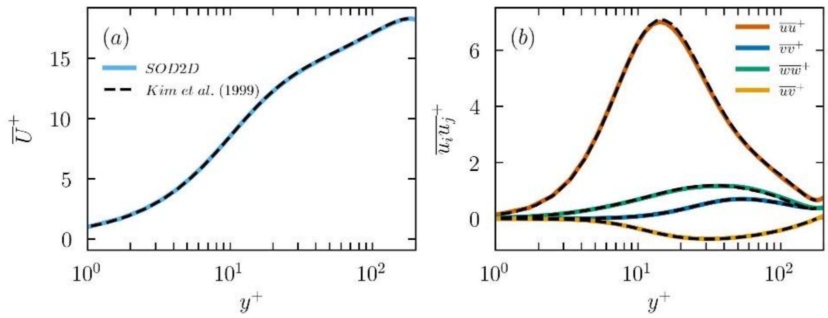

Figure 4: Turbulent statistics in a turbulent channel flow at $\boldsymbol{Re_\tau = 180}$ simulated with SOD2D and compared with the reference by Kim et al. (1987).

Turbulent Boundary Layers simulated in SOD2D. Wall-bounded flows, in general, are subjected to pressure variations due to surface curvature or an external forcing. When the free-stream pressure increases in the flow direction, the resulting adverse pressure gradient slows down the flow leading to flow separation. For an aircraft, the adverse pressure gradient acting on its wings' surface can result in stall and increased drag at high angle of attacks. Simple flow configurations as turbulent boundary layers over isothermal flat plates can be regarded as a good starting point for studying more complex flow configurations involving pressure gradients. In this context, we developed a flat-plate boundary layer class in SOD2D code that can simulate the zero- and adverse-pressure-gradient boundary layer flows. In the BL setup, the laminar Blasius profile at a given Reynolds number is injected at the inlet, and flow is let to develop along the flat plate. To trigger faster laminar-turbulent transition, a weak random volume force tripping procedure is implemented. Figure 5 presents a snapshot of the flow field in the zero-pressure gradient turbulent boundary layer.

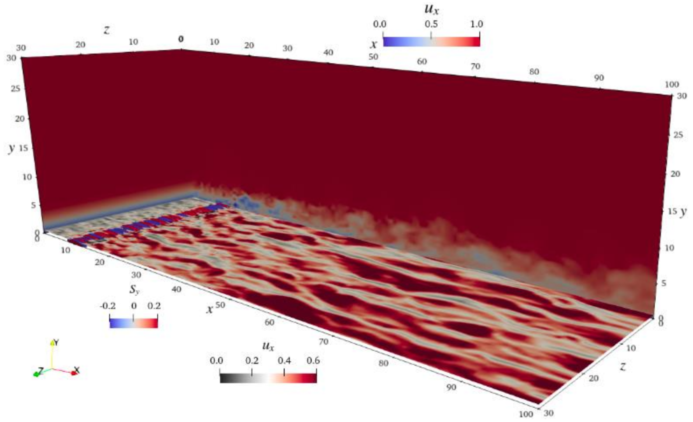

Figure 5: Instantaneous visualization of a zero-pressure-gradient turbulent boundary layer simulated with SOD2D.

References

M. Atzori, P. Torres, A. Vidal, S. Le Clainche, S. Hoyas and R. Vinuesa. High-resolution simulations of a turbulent boundary layer impacting two obstacles in tandem. Phys. Rev. Fluids, 8, 063801, 2023.

Dong, S., Karniadakis, G.E., Chryssostomidis, C., 2014. A robust and accurate outflow boundary condition for incompressible flow simulations on severely-truncated unbounded domains. J. Comput. Phys. 261, 83–105.

Fischer, P. F., Lottes, J. W., Kerkemeier, S. G., 2008. NEK5000: Open source spectral element CFD solver. Available at: http://nek5000.mcs.anl.gov.

J. Kim, P. Moin and R. Moser. Turbulence statistics in fully developed channel flow at low Reynolds number. J. Fluid Mech. 177, 133-166 (1987)

Lelieveld, J.; Klingmüller, K.; Pozzer, A.; Pöschl, U.; Fnais, M.; Daiber, A.; Münzel, T. Cardiovascular disease burden from ambient air pollution in Europe reassessed using novel hazard ratio functions. Eur. Heart J. 2019, 40, 1590–1596.

A. Martinez-Sanchez, E. López, S. Le Clainche, A. Lozano-Durán, A. Srivastava and R. Vinuesa. Causality analysis of large-scale structures in the flow around a wall-mounted square cylinder. J. Fluid Mech., 967, A1, 2023.

A. T. Patera, A spectral element method for fluid dynamics: laminar flow in a channel expansion, J. Comput. Phys. 54 (1984), pp. 468–488.

P. Torres, S. Le Clainche and R. Vinuesa. On the experimental, numerical and data-driven methods to study urban flows. Energies, 14, 1310, 2021.